Original Research

Susceptibility Weighted Imaging With Multiple Echoes

Christian Denk, BSc and Alexander Rauscher, PhD*

Purpose: To extend susceptibility weighted imaging (SWI) to multiple echoes with an adapted homodyne filtering of phase images for the computation of venograms with improved signal to noise ratio (SNR) and contrast to noise ratio (CNR) and to produce high resolution maps of R_2^* relaxation.

Materials and Methods: Three-dimensional multi echo gradient echo data were acquired with five equidistant echoes ranging from 13 to 41 ms. The phase images of each echo were filtered with filter parameters adjusted to the echo time, converted into a phase mask, and combined with the corresponding magnitude images to obtain susceptibility weighted images. The individual images were then averaged. Conventional single echo data were acquired for comparison. Maps of R_2^* relaxation rates were computed from the magnitude data. Field maps derived from the phase data were used to correct R_2^* for the influences from background inhomogeneities of the static magnetic field.

Results: Compared with the single echo images, the combined images had an increase in SNR by 46% and an improvement in CNR by 34 to 80%, improved visibility of small venous vessels and reduced blurring along the readout direction. The R_2^* values of different tissue types are in good agreement with values from the literature.

Conclusion: Acquisition of SWI with multiple echoes leads to an increase in SNR and CNR and it allows the computation of high resolution maps of R_2^* relaxation.

Key Words: magnetic susceptibility; phase; brain; MRI; R_2^*; relaxation
J. Magn. Reson. Imaging 2010;31:185–191.
© 2009 Wiley-Liss, Inc.

GRADIENT ECHO (GRE) techniques are widely used in MRI. Applications include, among others, vascular imaging, three-dimensional (3D) volume imaging and heavily T_2^* weighted imaging. Gradient echo imaging is fast and it has low specific absorption rates due to small flip angles and the absence of refocusing pulses. The T_2^* relaxation time is very sensitive to changes in magnetic susceptibility. Iron as a source of susceptibility variations is of particular interest (1), because it is a potential marker for pathologies such as Parkinson disease (2,3), Huntington disease (4), Alzheimer disease (5), and multiple sclerosis (6,7). The T_2^* decay is sensitive not only to tissue properties but also to background field inhomogeneities generated by air–tissue and bone–tissue interfaces or by imperfect shim. Therefore, the measured decay also depends on imaging parameters such as voxel size and slice orientation. The decay can be corrected for the unwanted influence from background inhomogeneities (8,9). Multi echo GRE imaging has been used to probe brain tissue for its iron content (10) and even for its myelin content (11).

Susceptibility weighted imaging (SWI) is a single echo 3D gradient echo sequence with high spatial resolution and long echo time (TE). What distinguishes SWI from conventional GRE imaging is that the phase of the signal is incorporated to obtain images with improved contrast. The phase contains valuable information (12) and has a higher signal to noise ratio (SNR) compared with the corresponding magnitude (13). Both magnitude and phase of the susceptibility weighted data are sensitive to local variations in tissue magnetic susceptibility. These changes in the magnetic field are mapped into the phase's limited domain ($-\pi \leq \phi < \pi$). The resulting ambiguities are usually referred to as phase wraps. The field inhomogeneities and, therefore, the number of phase wraps scale with field strength and with echo time. The elimination of phase wraps is either performed by phase unwrapping (14,15) or by homodyne filtering (16). Phase unwrapping preserves all spatial frequencies. The homodyne filter, on the other hand, is a low pass filter implemented in k-space, usually as a 2D Hanning window. Complex division of the original image by the filtered image results in a high pass filtered image. In this image, the influences from background inhomogeneities and phase wraps are suppressed.

For SWI at 1.5T with a TE of 40 ms, it was found that a window width of approximately 20 to 25% of the respective k-space dimension results in sufficient phase wrap suppression and good susceptibility contrast [17]. The susceptibility weighted phase can be used to assess brain iron content [18] and to visualize brain anatomy in high detail [12,13].

Because both T_2^* and phase have the potential to assess brain iron content it seems a worthwhile goal to acquire both types of information in one scan. The aim of this work was, therefore, to combine quantitative T_2^* measurements with the capabilities of SWI. SWI was thus acquired with multiple echoes. The phase correction by homodyne filtering was optimized for each individual echo by adapting the size of the filter window. Maps of $R_2^* = 1/T_2^*$ relaxation were computed from the magnitude of the data. The phase was used to compute field maps to correct the R_2^* maps for background inhomogeneities. SNR and contrast to noise ratio (CNR) were compared between single echo SWI and the proposed multi echo technique.

MATERIALS AND METHODS

Data Acquisition

Data from four healthy volunteers with no history of neurological or psychiatric diseases were acquired after obtaining informed written consent. Multi echo SWI data were acquired on a Philips Achieva 3T system equipped with an 8 channel head coil using a 3D gradient echo sequence. Five echoes with TE ranging from 13 to 41 ms and an interval of 7 ms were acquired with gradients of alternating polarity [19]. The first echo is fully flow compensated, whereas the third and fifth echo are flow compensated only in readout direction. Due to the sequence configuration, there is no flow compensation on the second and fourth echo. Further scan parameters were as follows: repetition time (TR) = 45 ms, flip angle (FA) = 17° and a readout bandwidth of 157 Hz/pixel; field of view (FOV) = 210 × 60 × 160 mm^3; spatial resolution = 0.5 × 0.75 × 1.5 mm^3 (voxel volume = 0.56 mm^3) for the acquisition and 0.41 × 0.41 × 0.75 mm^3 for the reconstruction with a matrix of 512 × 512 × 80 voxels. The average scan duration was 6.7 min. For comparison of SNR and CNR, a single echo scan with the same spatial resolution (TE = 20 ms, TR = 45 ms, FA = 17°, readout BW = 110 Hz/pixel, acquisition time 6.6 minutes) was acquired. In one subject, an additional scan with a spatial resolution of 0.4 × 0.6 × 1.5 mm^3 (voxel volume = 0.36 mm^3) was acquired and reconstructed to 0.32 × 0.32 × 0.75 mm.

To investigate the effects of different sizes of the homodyne filter window, data from a spherical phantom were acquired. Macroscopic field inhomogeneities were generated by a 20-mL bottle containing a gadolinium contrast agent (0.5 mmol/mL) which was placed adjacent to the spherical phantom.

Data Processing Analysis

All image processing was performed using MATLAB (The MathWorks, Inc., Natick, MA) and FSL (FMRIB, Oxford, UK) on a personal computer with 8 Gb of memory running GNU/Linux. Magnitude and phase of the data were reconstructed on the MRI scanner using Sensitivity Encoding (SENSE) [20].

For SWI processing [21,22] a symmetrically centered 2D Hanning low pass frequency filter was applied in a slice by slice manner to the 2D k-space data. For TE = 20 ms, a filterwidth (FW) of 0.25 of the k-space dimension was used. With increasing TE the spatial density of phase wraps increases. Thus, FW adaption for different TE was explored. The FW of 0.25 at TE = 20 ms was used as a reference [17]. For longer TE, the FW was increased so that the residual phase wraps were comparable to the situation at TE = 20 ms. The low pass filtered phase images were subtracted form the original phase images using complex division to produce high pass filtered phase images. The assessment of the filter effect was based on visual inspection of the resulting phase images. The filtered phase images were converted into a negative phase mask. The fourth power of the mask was multiplied with the corresponding magnitude images to obtain the final SWI for each individual echo [21,22]. Finally, the SWI of the five echoes were averaged.

R_2^* Maps

Maps of R_2^* relaxation rates were computed from the five magnitude images using a Levenberg-Marquardt least squares method for nonlinear equations. To correct for signal decay due background field inhomogeneities the method proposed by Fernández-Seara and Wehrli [8] and extended by Dahnke and Schaeffter [9], was used, which assumes a constant gradient in through plane direction. The field map required for this approach was computed from the unwrapped phase $\Delta\tilde{\varphi}$ $(\mathrm{TE}_{i+1}, \mathrm{TE}_i)$ using the ΦUn tool [14] of the complex division of data from subsequent echo times TE_{i+1} and TE_i:

$$\Delta B_{i,i+1} = \frac{1}{\gamma(\mathrm{TE}_{i+1} - \mathrm{TE}_i)} \cdot \Delta\tilde{\varphi}, \qquad [1]$$

where gamma is the gyromagnetic ratio of the proton. To improve SNR of the field map, the average of the four possible $\Delta B_{i,i+1}$ was computed.

R_2^* was computed by fitting the following Equation.

$$S_{\Delta B_0}(\mathrm{TE}) = S_0 \cdot e^{-\mathrm{TE} \cdot R_2^*} \cdot \left| \frac{\sin(\gamma \cdot \Delta B_0)/(2 \cdot \mathrm{TE})}{\gamma \cdot \Delta B_0/(2 \cdot \mathrm{TE})} \right|, \qquad [2]$$

where $S_{\Delta B_0}(\mathrm{TE})$ is the magnitude signal intensity at TE; S_0 is the signal intensity at TE = 0; and ΔB_0 is the linear field variation. The sinc-term component in Eq. [2] is used for the correction of the influence from background field inhomogeneities.

Comparison of SNR and CNR Between Single and Multi Echo SWI

The single echo data were coregistered to the multi echo data using FSL by first registering the magnitude
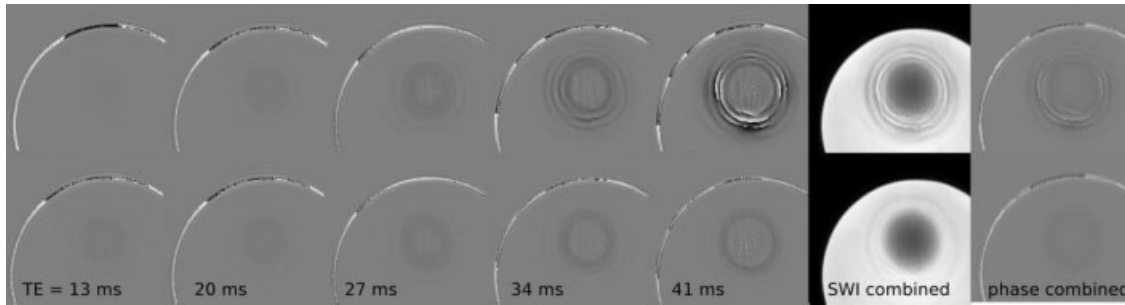
Figure 1. Filtered phase images for the first to the fifth echo computed with a constant filter width of 0.25 (top row) and adapted filter widths ranging from FW = 0.2 at 13 ms to FW = 0.4 at 41 ms with increments of 0.05 (bottom row). With the constant filter width phase wraps are present in the later echo times (34 and 41 ms) and in the combined phase and SWI, whereas the adapted filter successfully reduces phase wraps at all echo times. Note that the strong field inhomogeneities lead to signal loss in the magnitude due to intravoxel spin dephasing, which becomes apparent in the final SWI images.

and then applying the registration parameters to the real and the imaginary part of the data. Phase images and SWI were then reconstructed from the registered complex data. SNR and CNR were determined for the single echo data and the combined magnitude images of the multi echo data. SNR was determined in six different regions in white matter (WM). SNR increase was calculated for each region separately and then averaged. CNR was defined as the signal intensity differences between two neighboring tissue types, divided by the standard deviation of noise. CNR was evaluated between WM and the following structures: gray matter (GM), putamen, corpus callosum, optic radiation and veins. The standard deviation of a different region in the corpus callosum was used as a measure of noise.

RESULTS

The effects of constant versus adaptive homodyne filtering are shown in Figures 1 (phantom) and 2 (in vivo). With the standard filter width of 0.25 for all echo times phase wraps started to appear at a TE of 34 ms and degrade the final SW image. Adapted filter widths ranging from 0.2 at TE = 13 ms to 0.4 at TE = 41 ms with increments of 0.05 for every additional 7 ms (FW = 0.05/7 * TE + 0.107) resulted in good suppression of phase wraps and good phase contrast. With the adaptive filter the susceptibility contrast in the phase was similar for all echo times (Figure 2).

Combined multi echo magnitude images had better SNR and CNR than their single echo counterpart (Figure 3 and Table 1). Small veins were better visible and less blurred in the multi echo images than in the
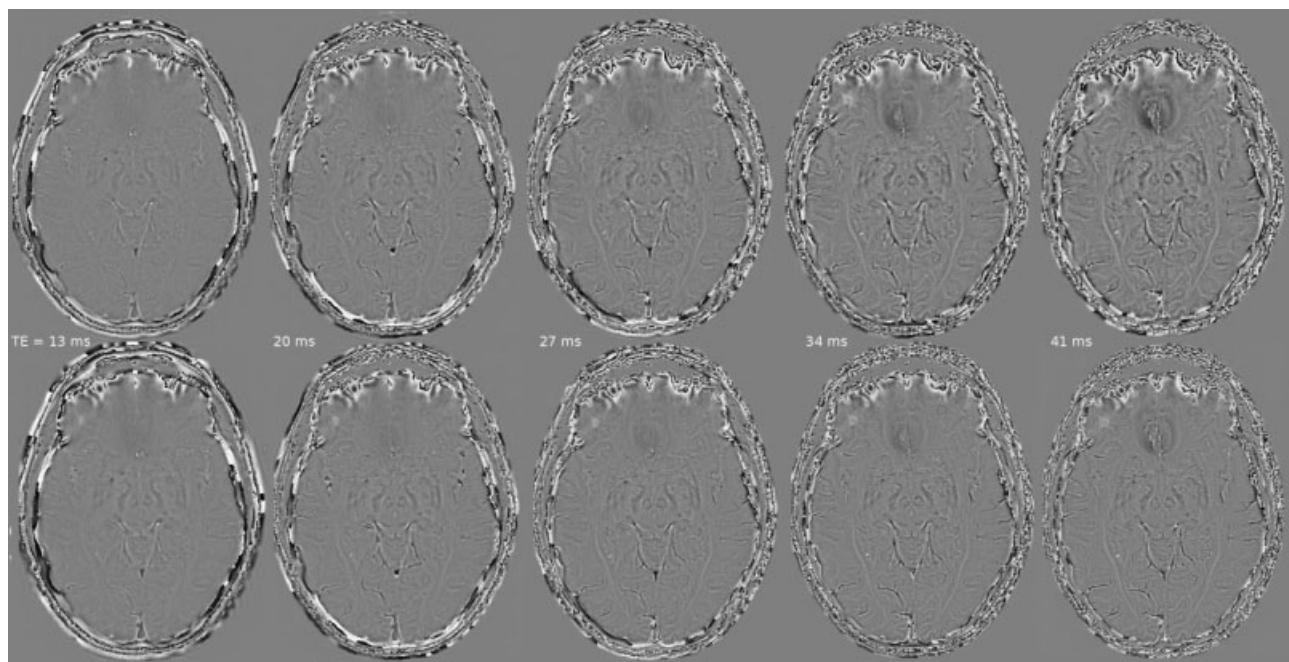
Figure 2. Phase images of the first to the fifth echo produced with a constant width of the homodyne filter (top row) and filter widths adjusted to the echo times (bottom row). Adaptation of the filter width (FW = 0.2 at 13 ms to FW = 0.4 at 41 ms with increments of 0.05) results in a reduction of residual phase wraps.
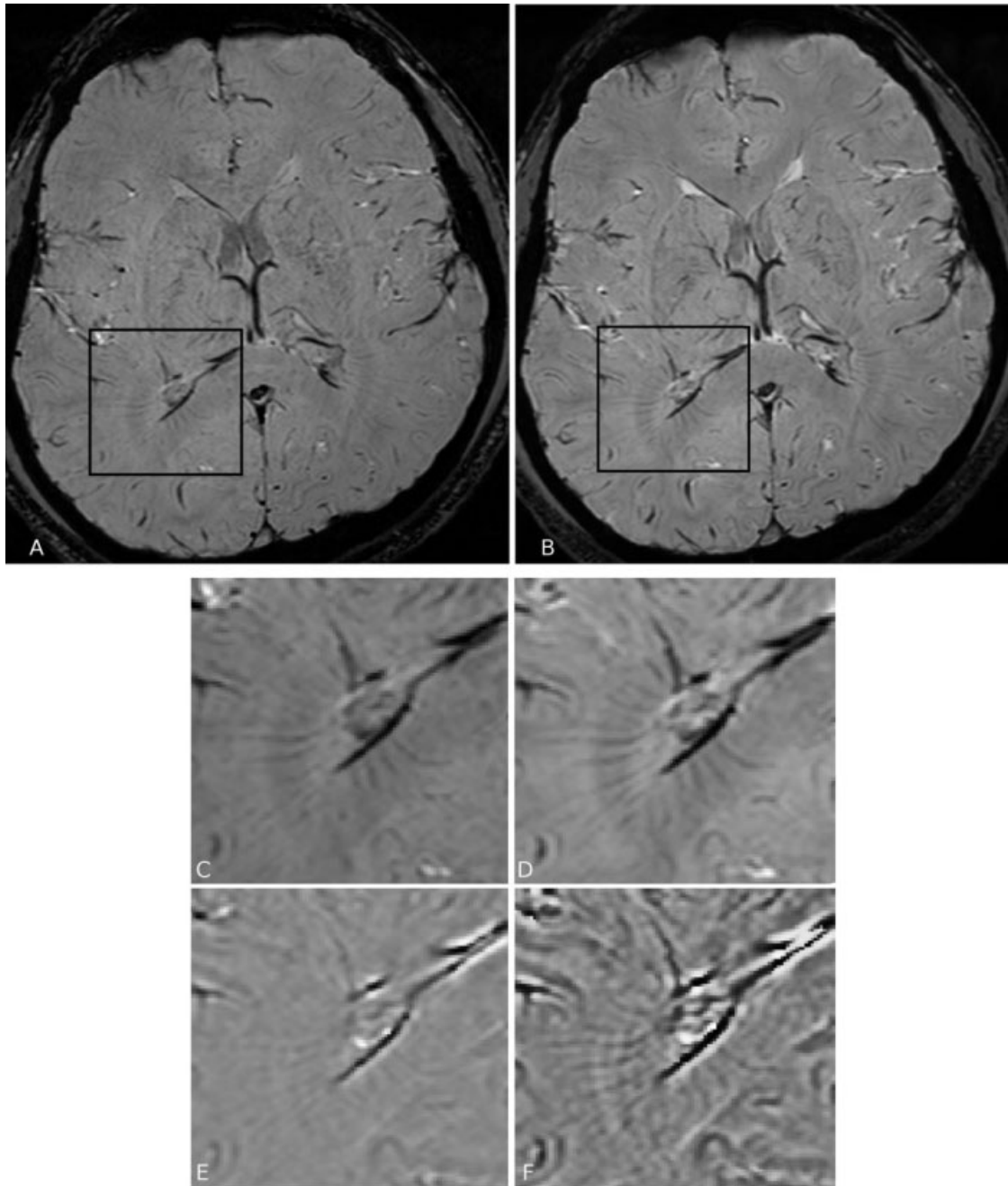
Figure 3. One slice of the single echo SWI (**A**) and the combined five-echo SWI (**B**). The zoomed areas show magnitude and phase of the single echo data (magnitude in **C**, phase in **E**) and the combined multi echo data (magnitude in **D**, phase in **F**). Visibility of small veins, SNR and CNR are improved in the multi echo data (D,F) compared with the single echo images (C,E). Signal dropout in the frontal regions is slightly increased in the multi echo image. CSF in the SWI multi echo appears brighter, due to their short T_2^*.

single echo images. SNR increased by approximately 50% and CNR increased by 34 to 80%, depending on the tissue type (Table 1). R_2^* values from Péran et al (23), Du et al (24), and Krüger and Glover (25) have been presented in Table 1 to compare them with our findings.

Minimum intensity projections over 7.5 mm of the magnitude, the phase, the venogram and the R_2^* of the high resolution scan are shown in Figure 4. The R_2^* map (Figure 4D) and the phase image (Figure 4B) displayed the best contrast between GM and WM. The

values for R_2^* ranged between 15 s^{-1} in GM and 47 s^{-1} in the optic radiation. Areas of large R_2^* (bright) coincided with venous vessels visible in the venograms.

DISCUSSION

Susceptibility weighted imaging with a multi echo approach offers a variety of advantages over the single echo technique. Conventional SWI uses a low readout

Table 1
CNR, SNR Increase and R_2^* Values for Different Tissue Types

| | CNR [%] | SNR [%] | R_2^* [10^{-3} ms^{-1}] | R_2^* Literature values | | |
				Perán et al 2007	Du et al. 2009	Krüger and Glover 2001
white matter	–	46 ± 54	19.7 ± 1.1	18.7 ± 1.7	L: 23.0 ± 5.5 R: 22.3 ± 5.2	20.4 ± 1.2
gray matter	37 ± 49	–	15.26 ± 2.1	14.2 ± 3.9	–	21.6 ± 1.7
putamen	75 ± 137	–	27.1 ± 1.0	25.1 ± 2.2	L: 29.0 ± 8.9 R: 31.3 ± 10.4	–
corpus callosum	66 ± 49	–	23.9 ± 1.0	–	–	–
optic radiation	80 ± 123	–	21.1 ± 1.0	–	–	–
veins	34 ± 50	–	47.3 ± 8	–	–	–

Values given in format mean ± standard deviation
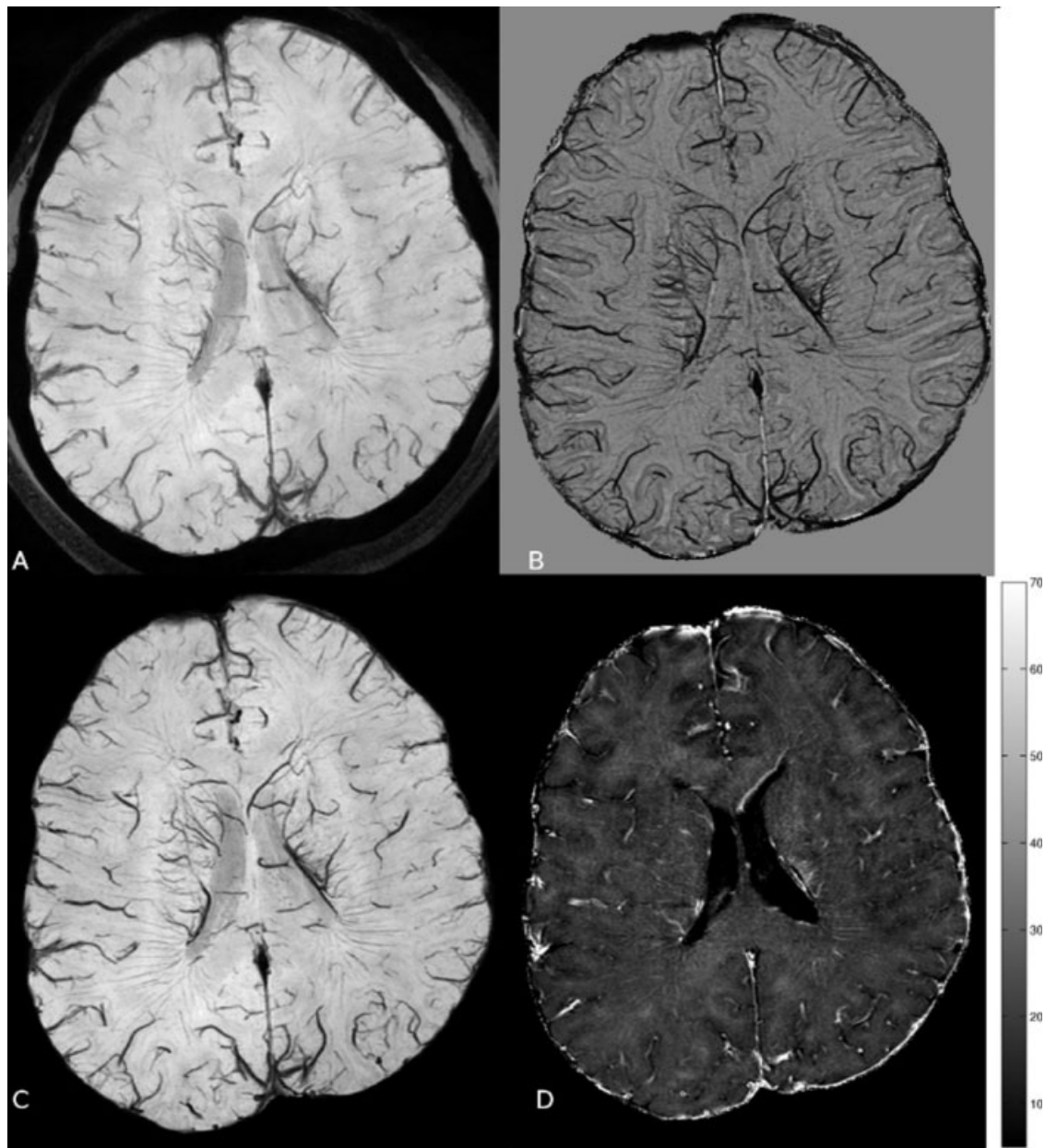
Figure 4. Minimum intensity projections over 7.5 mm (10 slices) of the magnitude (**A**), the phase (**B**), and the SWI (**C**) of the combined five echoes of the high resolution scan (voxel size 0.32 × 0.32 × 0.75 mm). The R_2^* map of the center slice of the stack is shown in **D**. Small subependymal veins are visible in all four images. Contrast between gray matter and white matter is best in the phase image and in the R_2^* map.

bandwidth to improve SNR. This is necessary because of the small voxel sizes and it is possible because of the long echo times. The increased bandwidth required for the relatively short interecho delay of 7 ms in our multi echo method results in a reduction of geometric distortions, smaller chemical shifts and reduced blurring along the readout direction. The resulting SNR penalty per echo is more than compensated by the acquisition of several echoes. The total data acquisition length (number of echoes divided by the readout bandwidth in Hz/pixel) of the multi echo sequence is 32 ms compared with 9 ms for single echo data. Moreover, maps of R_2^* relaxation can be computed.

One caveat is that only the first echo is fully flow compensated. The second and the fourth echo are not flow compensated, and the third and fifth echo are only flow compensated along the readout direction (19). Large arterial vessels may, therefore, experience signal loss due to fast flow and could be mistaken for veins in the later echoes.

SWI benefits from the reconstruction of multi channel data using the SENSE algorithm (20), which results in unfiltered (but not unwrapped) phase images. Both unwrapping and homodyne filtering can be performed on these images. Homodyne filtering is a robust technique for the generation of high pass filtered phase images. In contrast to standard SWI processing with a fixed filter width for different echo times, we adjusted the homodyne filter to account for the increased spatial density of phase wraps at later echo times. Deistung et al (17) investigated the influence of different parameters of the homodyne filter at 1.5T at an echo time of 40 to 50 ms. They reported that a 2D filter window in k-space with a size of 20 to 25% of the respective k-space dimension leads to good phase contrast and suppression of phase wraps. Because the phase associated with field inhomogeneities scales linearly with $B_0 \times TE$, we used a filter size of 0.25 at the TE of 20 ms and adjusted the size according to the other echo times. This resulted in the expected reduction of phase wraps in the images acquired at later echo times.

The correction of R_2^* for background field inhomogeneities requires unfiltered phase images where all spatial frequencies are preserved. If the phase does not wrap during the time between two echoes, the field map can be computed directly by the complex division of two subsequent echoes. In this study, an interecho delay of 7 ms was used to allow for high spatial resolution and to cover a broad range of echo times. Long interecho delays result in good SNR of the field maps (26) but also in phase wraps in areas with strong background inhomogeneities which have to be removed by phase unwrapping.

The R_2^* values determined with our high resolution five-echo method are in good agreement with the values reported in the literature (23–25). It should be mentioned that the concept of R_2^* fails near venous vessels because R_2^* is only defined for an exponential decay. Because the frequency distribution around a venous vessel is non-Lorentzian, the decay is nonexponential and even a partial signal recovery can occur

at late echo times (27). This fact and that vessel orientation and partial volume effects have a strong influence on the signal formation around a vein (27) explain the large standard deviation of the "R_2^*" of venous vessels observed in this study. For the computation of R_2^* maps, full flow compensation is not relevant because R_2^* is not defined in these regions, since the decay due to field inhomogeneities associated with veins is not exponential (27). That our technique provides venograms perfectly coregistered with the R_2^* maps allows the exclusion of larger veins from region of interest based analysis.

The strong increase in SNR and CNR compared with the single echo magnitude images should be interpreted carefully because SNR measurements are difficult to perform in images obtained with phased array coils (20). It is impossible to obtain a reliable noise measurement by placing a region of interest into the background of images acquired with phased array coils. Therefore, we computed the standard deviation of a region placed in white matter, assuming that the signal variation due to tissue heterogeneity is constant over the different echo times. No absolute SNR values can be determined with this approach, but because the same regions were used in the magnitude images in the single echo data and in the multi echo data, at least a qualitative comparison is feasible. Moreover, we found only minor variations in the standard deviation for the same noise region at the five echo times. Despite these limitations, an increase in SNR and CNR was found in all regions of interest. Although no definite quantitative values can be given, the SNR and CNR increase in all evaluated regions is in good agreement with the overall visual impression of the images. The increase in SNR found in this study is also in agreement with a study by Brainovich et al (28) who found an increase in SNR by 48% in dual echo SWI compared with the single echo method using a bird cage head coil at 3T and a readout bandwidth of 79 Hz/pixel for both echoes. Recently Helms and Dechent (29) presented a thorough investigation of the effects of multi echo averaging. One of their conclusions was that sampling beyond 25 ms is not recommended because background inhomogeneities cause considerable signal drop out in the orbitofrontal cortex. This is true for the voxel sizes used in typical GRE (1–2 mm^3). SWI, on the other hand, acquires data with a voxel size of 0.5 mm^3 or smaller. The influence of background gradients is, therefore, reduced compared with lower spatial resolutions (30) allowing for longer echo times.

In conclusion this technique allow the computation of high quality venograms, phase images with high contrast, field maps and high resolution R_2^* maps. The proposed technique comes at almost no cost in terms of data acquisition time and it allows for a joint analysis of R_2^* and phase at high spatial resolution.

ACKNOWLEDGMENT

REFERENCES

1. Schenck JF, Zimmerman EA. High-field magnetic resonance imaging of brain iron: birth of a biomarker? NMR Biomed 2004; 17:433–445.
2. Berg D, Hochstrasser H, Schweitzer KJ, Riess O. Disturbance of iron metabolism in Parkinson's disease—ultrasonography as a biomarker. Neurotox Res 2006;9:1–13.
3. Griffiths PD, Dobson BR, Jones GR, Clarke DT. Iron in the basal ganglia in Parkinson's disease. An in vitro study using extended X-ray absorption fine structure and cryo-electron microscopy. Brain 1999;122:667–673.
4. Bartzokis G, Cummings J, Perlman S, Hance DB, Mintz J. Increased basal ganglia iron levels in Huntington disease. Arch Neurol 1999;56:569–574.
5. Morris CM, Kerwin JM, Edwardson JA. Non-haem iron histo-chemistry of the normal and Alzheimer's disease hippocampus. Neurodegeneration 1994;3:267–275.
6. Levine SM. The role of iron in the pathogenesis of experimental allergic encephalomyelitis and multiple sclerosis. Ann NY Acad Sci 2004;1012:252–266.
7. Zamboni P. The big idea: iron-dependent inflammation in venous disease and proposed parallels in multiple sclerosis. J R Soc Med 2006;99:589–593.
8. Fernández-Seara MA, Wehrli FW. Post processing technique to correct for background gradients in image-based R_2^* measurements. Magn Reson Med 2000;44:358–366.
9. Dahnke H, Schaeffter T. Limits of detection of SPIO at 3.0 T using T_2 relaxometry. Magn Reson Med 2005;53:1202–1206.
10. Martin WRW, Wieler M, Gee M. Midbrain iron content in early Parkinson disease: a potential biomarker of disease status. Neurology 2008;70:1411–1417.
11. Du YP, Chu R, Hwang D, et al. Fast multislice mapping of the myelin water fraction using multicompartment analysis of T_2^* decay at 3T: a preliminary postmortem study. Magn Reson Med 2007;58:865–870.
12. Rauscher A, Sedlacik J, Barth M, Mentzel H, Reichenbach JR. Magnetic susceptibility-weighted MR phase imaging of the human brain. AJNR Am J Neuroradiol 2005;26:736–742.
13. Duyn JH, van Gelderen P, Li T, et al. High-field MRI of brain cortical substructure based on signal phase. Proc Natl Acad Sci USA 2007;104:11796–11801.
14. Witoszynskyj S, Rauscher A, Reichenbach JR, Barth M. Phase unwrapping of MR images using Phi UN - a fast and robust region growing algorithm. Med Image Anal 2009;13:257–268.
15. Chavez S, Xiang Q, An L. Understanding phase maps in MRI: a new cutline phase unwrapping method. IEEE Trans Med Imaging 2002;21:966–977.
16. Noll DC, Nishimura DG, Macovski A. Homodyne detection in magnetic resonance imaging. IEEE Trans Med Imaging 1991;10: 154–163.
17. Deistung A, Rauscher A, Sedlacik J, Witoszynskyj S, Reichenbach JR. Optimization of data processing in susceptibility weighted imaging. In: Proceedings of the 14th International Conference of Medical Physics, Nuremberg, Germany, 2005. p 1168–1169.
18. Ogg RJ, Langston JW, Haacke EM, Steen RG, Taylor JS. The correlation between phase shifts in gradient-echo MR images and regional brain iron concentration. Magn Reson Imaging 1999;17: 1141–1148.
19. Deistung A, Dittrich E, Sedlacik J, Rauscher A, Reichenbach JR. ToF-SWI: simultaneous time of flight and fully flow compensated susceptibility weighted imaging. J Magn Reson Imaging 2009;29: 1478–1484.
20. Pruessmann KP, Weiger M, Scheidegger MB, Boesiger P. SENSE: sensitivity encoding for fast MRI. Magn Reson Med 1999;42: 952–962.
21. Reichenbach JR, Venkatesan R, Schillinger DJ, Kido DK, Haacke EM. Small vessels in the human brain: MR venography with deoxyhemoglobin as an intrinsic contrast agent. Radiology 1997; 204:272–277.
22. Haacke EM, Xu Y, Cheng YN, Reichenbach JR. Susceptibility weighted imaging (SWI). Magn Reson Med 2004;52:612–618.
23. Péran P, Hagberg G, Luccichenti G, et al. Voxel-based analysis of R_2^* maps in the healthy human brain. J Magn Reson Imaging 2007;26:1413–1420.
24. Du YP, Jin Y, Hu Y, Tanabe J. Multi-echo acquisition of MR angiography and venography of the brain at 3 Tesla. J Magn Reson Imaging 2009;30:449–454.
25. Krüger G, Glover GH. Physiological noise in oxygenation-sensitive magnetic resonance imaging. Magn Reson Med 2001;46:631–637.
26. Hutton C, Bork A, Josephs O, et al. Image distortion correction in fMRI: a quantitative evaluation. Neuroimage 2002;16:217–240.
27. Sedlacik J, Rauscher A, Reichenbach JR. Obtaining blood oxygenation levels from MR signal behaviour in the presence of single venous vessels. Magn Reson Med 2007;58:1035–1044.
28. Brainovich V, Sabatini U, Hagberg GE. Advantages of using multiple-echo image combination and asymmetric triangular phase masking in magnetic resonance venography at 3 T. Magn Reson Imaging 2009;27:23–37.
29. Helms G, Dechent P. Increased SNR and reduced distortions by averaging multiple gradient echo signals in 3D FLASH imaging of the human brain at 3T. J Magn Reson Imaging 2009;29:198–204.
30. Reichenbach JR, Venkatesan R, Yablonskiy DA, et al. Theory and application of static field inhomogeneity effects in gradient-echo imaging. J Magn Reson Imaging 1997;7:266–279.